

# *Dynamic Analysis of Turbocharger Rotor System*

**Kami Mou**

*Chengdu Foreign Languages School, 35 Baicao Rd, Pidu, Chengdu, Sichuan, China*

**Keywords:** Turbocharger rotor system (TRS), Capone nonlinear oil force, Bearing, Lubrication, Centralized mass model, Dynamic analysis

**Abstract:** The Turbocharge Rotor System (TRS) is a key component for enhancing engine performance. However, grasping its intricate dynamic response poses a formidable challenge for modeling and analysis. This study explores the optimal parameters for the dynamic operation of a TRS. To achieve this, we employ the Jeffcott Rotor System Model and Concentrated Mass Model for dynamic modeling of TRS, and the Capone model for calculating the nonlinear oil lubrication forces. The dynamic model of the TRS was solved using in-house built MATLAB codes, followed by a parametric study to reveal the influence of specific parameters on the dynamic performance of the TRS. This study ultimately provides us with the optimal values of these parameters, which can be valuable for guiding the design and optimization of TRS in practical scenarios. Top of Form

## 1. Introduction



Figure 1: Formula 1 Racing (Baidu.com)

F1 Shanghai Grand Prix, which is an influential event in China every year. As a local citizen, this ignited a profound interest in this sport, prompting me to delve deeper into its intricacies, as shown in Fig 1. What particularly captivated was the intricately designed engine systems of these vehicles, leading me to focus my studies on the turbocharger rotor system (TRS) within them. Within this engineering marvel, the TRS stands as a testament to innovation, power, and precision. However, this sophisticated system does not come without its challenges. As automotive technology continues to advance, researchers are faced with the formidable task of unraveling its complexities.

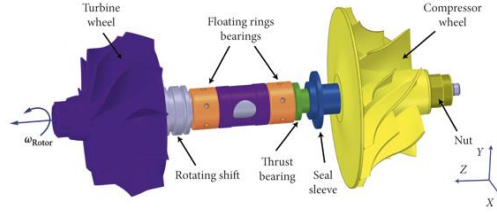


Figure 2: Model of Turbocharger Rotor System [1]

The TRS (Fig 2) is the key component at the heart of a high-performance engine, playing a vital role in extracting maximum power efficiency from each drop of fuel. Yet, with the increasing sophistication of engines and the growing demands for efficiency and performance, the imperative of comprehending and addressing the persistent challenges posed by this pivotal system becomes ever more pronounced. Achieving optimal performance necessitates a comprehensive understanding of the challenges faced by turbocharger rotor systems, spanning from heat stress and oil contamination issues to energy imbalances and material fatigue. Engine is the core power source for a multitude of machinery, dictating the power performance of planes, ships, vehicles and many other key machines. Turbocharger is a crucial technique for enhancing engine efficiency, particularly vital racing cars where the dynamic behavior of turbocharger system dictates the actual performance. Due to the unique characteristics of the turbocharger system, its dynamic behavior often exhibits chaotic tendencies during operation, potentially impacting the stable operation of the turbocharger. In China, research on turbocharger system started late and heavily relied on empirical trial-and-error methods and reverse engineering. Given the escalating international tensions among nations, an in-depth study of dynamic behavior of TRS is now an urgent national priority, carrying significant practical significance.

In recent years, turbochargers have seen increased utilization in diesel-powered maritime applications, locomotives, and the automotive industry. Furthermore, they are frequently employed in aeronautical applications to improve engine performance. While turbochargers used in marine and locomotive applications are considerably larger in scale, boasting rotational speeds around 30,000 rpm, the lightweight turbochargers utilized in the aerospace and automotive industries surpass 150,000 rpm in rotational velocity. These turbochargers augment engine performance and reduce emissions by elevating the engine's mass and incoming air pressure, while concurrently harnessing waste energy from exhaust gases. For turbochargers, which operate at higher speeds and exhibit strong nonlinearity, they are typically supported by various types of bearings, including floating ring bearings, rolling element bearings, hydrodynamic bearings, and gas foil bearings. [4]

In this context, this paper embarks on a journey to contribute to the field of automotive engineering by providing a comprehensive analysis of turbocharger rotor system dynamics. Our objective is to shed light on the underlying mechanics governing the behavior of the turbocharger rotor system by examining these variables and their interrelationships. Additionally, this paper also endeavor to construct a new model for the dynamic behavior of turbocharger system, capable of precisely predicting dynamic responses across different rotational speed and analyzing the effects of various parameters on the system response. Through this effort, we wish to contribute to the growing knowledge base that fosters innovation in Formula 1 technology and, by extension, wider Automotive Industry.

As we delve deeper into this research, we are poised to gain insights that not only enhance our understanding of turbocharger and rotor design but also encapsulate the spirit of innovation driving Formula 1 racing. With each iteration, we advance closer to harness the full potential of this technology, pushing the boundaries of productivity and efficiency to new heights.

## 2. Theoretical Models

### 2.1 Jeffcott Rotor System Model

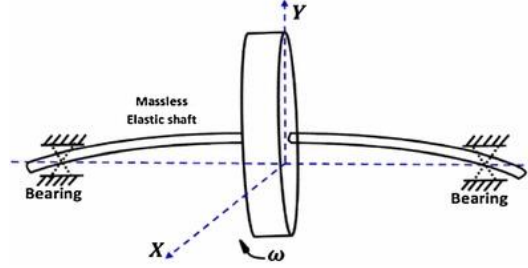


Figure 3: Illustration of Jeffcott Model for TRS [2]

The Jeffcott rotor model, named after its introducer, John Irwin Jeffcott, is a simplified representation of a rotating shaft widely used in engineering dynamics studies. It depicts a flexible shaft, usually represented as a massless rod, with its entire mass concentrated at a single point, as shown in Fig 3. This point symbolizes the rotor's components. The primary dynamic variable is the lateral displacement of the rotor from its central position. The model includes the effects of radial stiffness due to lateral forces, sometimes accounting for damping effects. Despite its simplicity and exclusion of all complexities of real systems, the Jeffcott rotor model provides valuable insights into fundamental rotor dynamics concepts. It aids in understanding vibration behavior, stability, and critical speeds in rotating machinery, despite its limitations, such as concentrating all mass at a single point, neglecting the shaft's mass, inertia, and gyroscopic effects, approximating the shaft's radial stiffness as linear, and considering a constant angular velocity.

Motor of the rotor can be described as:

$$\begin{cases} m_j \ddot{x}_j = f_{ix} + M_e \omega^2 \sin(\omega_j t) \\ m_j \ddot{y}_j = f_{iy} + M_e \omega^2 \cos(\omega_j t) + m_j g \end{cases}$$

Where  $m_j$  represents the mass of the system.  $x_j$  and  $y_j$  denote the displacement of the mass along the x-axis and y-axis, respectively, and they are denoted by  $x_j(t)$  and  $y_j(t)$ .  $\ddot{x}_j$  and  $\ddot{y}_j$  represent the acceleration along the x-axis and y-axis.  $f_{ix}$  and  $f_{iy}$  represent the lubrication force of the inner oil film along the x-axis and y-axis.  $M_e$  is product of eccentric mass and eccentric distance.  $\omega_j$  is rotation speed of the shaft.  $t$  represent time and  $g$  denotes the acceleration due to gravity.

The definition equations of bearing ring system for Jeffcott model are:

$$\begin{cases} m_r \ddot{x}_r = f_{ox} - f_{ix} \\ m_r \ddot{y}_r = f_{oy} - f_{iy} + m_r g \end{cases}$$

$m_r$  represents the mass of the ring.  $x_r$  and  $y_r$  represents the displacement of the system.  $\ddot{x}_r$  and  $\ddot{y}_r$  denote the second derivative of  $x_r$  and  $y_r$  with respect to time, representing the acceleration along the x-axis and the y-axis.  $f_{ox}$  and  $f_{oy}$  represent the lubrication force provided by the outer oil film to the ring in x and y directions, while  $f_{ix}$  and  $f_{iy}$  represent the lubrication force provided by the inner oil film to the ring surface in the x and y directions.

These equations describe how the single-degree-of-freedom mechanical system will respond and move under the influence of the external forces. Despite being oversimplified compared to more realistic models, the Jeffcott rotor model still captures several fundamental aspects of real-world rotors and provides a qualitative understanding of significant rotor dynamics events [5]. However, this model uses only a few parameters and offers a simple solution. The structure of the Jeffcott rotor

and the turbocharger rotor system differs significantly, with parameters being oversimplified. In addition, the model does not consider the elastic deformation of the rotor shaft. Consequently, achieving the required accuracy in the model's results can be challenging.

## 2.2 Capone Nonlinear Oil Film Force

When studying the dynamic characteristics of floating ring bearing rotor system, a large amount of result data is required. Consequently, a considerable number of oil film pressure solutions are required during the calculation process. Therefore, an efficient method for solving oil film pressure is needed, and in this study, the Capone nonlinear oil film pressure is adopted.

Earlier research frequently employed linear stiffness and damping coefficients to simulate the dynamic properties of bearings and seals [6], [7]. However, observations indicate significant nonlinearity in the fluid forces of bearings and seals. Additionally, in certain circumstances, such as when the journal experiences significantly disturbed motion, the linear model becomes inadequate for assessing the nonlinear dynamic behaviors of the rotor-bearing-seal system.

Various nonlinear oil-film force models have been proposed to more accurately represent the nonlinearity of sliding bearing's, as demonstrated in studies [8], [9], and [10].

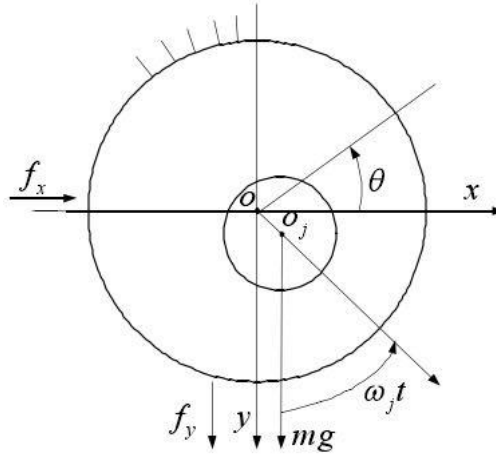


Figure 4: Cylindrical Bearing Diagram

Capone nonlinear oil film force models (Fig 4) the film thickness of cylindrical bearings as follows:

$$h = c - x \cos \theta - y \sin \theta$$

For general cylindrical bearings, the two-dimensional Reynolds equation is:

$$\frac{1}{R^2} \frac{\partial}{\partial \theta} \left( \frac{h^3}{\mu} \frac{\partial p}{\partial \theta} \right) + \frac{\partial}{\partial z} \left( \frac{h^3}{\mu} \frac{\partial p}{\partial z} \right) = 6\omega \frac{\partial h}{\partial \theta} + 12 \frac{\partial h}{\partial t} \quad (1)$$

It is simplified to a short bearing, in which the Reynolds equation has  $\frac{\partial p}{\partial z}$  and  $\frac{\partial p}{\partial \theta}$ , thus the formula (1) can be simplified to

$$\frac{\partial}{\partial z} \left( \frac{h^3}{\mu} \frac{\partial p}{\partial z} \right) = 6\omega \frac{\partial h}{\partial \theta} + 12 \frac{\partial h}{\partial t} \quad (2)$$

According to the oil film thickness formula, the second-order differential equation of oil film pressure can be derived from equation (2)

$$\frac{\partial^2 p}{\partial z^2} = \frac{6\mu}{h^3} [(\omega x - 2\dot{y}) \sin \theta - (\omega y + 2\dot{x}) \cos \theta] \quad (3)$$

The boundary condition of differential equation (3) stipulates that the pressure on both sides of the

bearing is zero:

$$p\left(\theta, z = +\frac{L}{2}\right) = p\left(\theta, z = -\frac{L}{2}\right) = 0 \quad (4)$$

According to the boundary condition (4), differential equation (3) can be integrated to obtain the expression for the oil film pressure, which is known as the Capone nonlinear oil film pressure:

$$p = \frac{3\mu}{h^3} \left( z^2 - \frac{L^2}{4} \right) [(\omega x - 2\dot{y}) \sin \theta - (\omega y + 2\dot{x}) \cos \theta] \quad (5)$$

### 2.2.1 Centralized Mass Model (CQM)

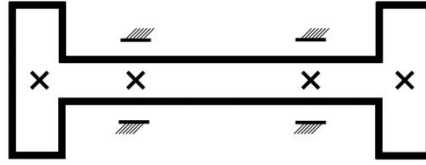


Figure 5: Centralized Mass Model Diagram

The Centralized Mass Model, also known as the Concentrated Mass Model, is an engineering simplification used to represent the dynamic behavior of complex mechanical systems, particularly those involving rotating machinery and structures. The Centralized Mass Model simplifies the turbocharger rotor system into four mass points, with each mass point connected by beams. This simplification is employed to analyze the overall motion and response of the system without considering the detailed distribution of mass or complexities in the structure.

Motion of the rotor system represented by the CQM can then be written as:

$$\begin{cases} M\ddot{X} + KX = F_{ox} + F_{ex} \\ M\ddot{Y} + KY = F_{oy} + F_{ey} - Mg \end{cases} \quad (6)$$

In this system of equations,  $M$  represents the mass of the system, as shown in the  $M$  matrix above.  $X$  represents the displacement along the x-axis, and  $Y$  represents the displacement along the y-axis.  $\ddot{X}$  and  $\ddot{Y}$  denote the second derivative of  $X$  and  $Y$  with respect to time, representing the acceleration along the x-axis and the y-axis.  $K$  the stiffness matrix of the rotor.  $F_{ox}$  and  $F_{oy}$  are the oil film force matrices in horizontal and vertical directions.  $F_{ex}$  and  $F_{ey}$  are the eccentric force matrices. The matrix equation does not include the four degrees of freedom of the floating ring because the floating ring is only affected by the oil film force and gravity, and the force form of the four nodes is different.

The matrix of mass is:

$$M = \begin{bmatrix} m_1 & 0 & 0 & 0 \\ 0 & m_2 & 0 & 0 \\ 0 & 0 & m_3 & 0 \\ 0 & 0 & 0 & m_4 \end{bmatrix}$$

If the stiffness coefficients of the three sections of the rotating shaft from left to right in Fig 5 are respectively  $k_1$ ,  $k_2$  and  $k_3$ , then the stiffness matrix of the rotor can be expressed as:

$$K = \begin{bmatrix} k_1 & -k_1 & 0 & 0 \\ -k_1 & k_1 + k_2 & -k_2 & 0 \\ 0 & -k_2 & k_2 + k_3 & -k_3 \\ 0 & 0 & -k_3 & k_3 \end{bmatrix}$$

Referring to the material mechanics data, it is evident that for simply supported beams, the transverse stiffness of beam is  $\frac{3EI}{l^3}$ , whereas for beams with fixed support, its transverse stiffness of beam is  $\frac{12EI}{l^3}$ . Thus, we have:

$$k_1 = k_3 = \frac{3EI}{l^3}, k_2 = \frac{12EI}{l^3}$$

Where  $E$  is the modulus of elasticity of the material, representing its ability to resist deformation, and  $I$  is the area moment of inertia of the beam's cross-section, quantifying how the area is distributed relative to the axis of bending.  $l$  represents the length of the beam.

It is necessary to analyze the force of the floating ring. The floating ring is subject to the gravity of the floating ring, the centrifugal force caused by the eccentricity of the floating ring weight, and the inner oil film force. However, since the weight of the floating ring is generally small, the eccentricity of the floating ring weight is relatively negligible. Therefore, in this study, we consider only the gravity of the floating ring and the forces from the inner and outer oil films. According to Newton's law, the force balance equation for the floating ring is:

$$\begin{cases} M_r \ddot{X}_r = F_{rox} - F_{rix} \\ M_r \ddot{Y}_r = F_{roy} - F_{riy} + M_r g \end{cases} \quad (7)$$

In this set of equations,  $M_r$  represents the matrix of mass of floating ring.  $X_r$  and  $Y_r$  represent the displacements along the x-axes and y-axes of ring, while  $\ddot{X}_r$  and  $\ddot{Y}_r$  represent the acceleration along the x-axis and y-axis.  $F_{rox}$  and  $F_{roy}$  are the component matrices of the outer oil film force acting on the floating ring in the x and y directions.  $F_{rix}$  and  $F_{riy}$  are the component matrices of the inner oil film force acting on the floating ring in the horizontal and the vertical directions, respectively.

During the solving process, it is necessary to assemble the coordinates of the floating ring and the four nodes.

Let the independent coordinate vector be:

$$q_x = [x_1 \quad x_2 \quad x_3 \quad x_4 \quad x_{r1} \quad x_{r2}]^T$$

$$q_y = [y_1 \quad y_2 \quad y_3 \quad y_4 \quad y_{r1} \quad y_{r2}]^T$$

The first four variables represent the independent coordinates of the four nodes, and the last two variables are the independent coordinates of the two floating rings. The total of independent coordinates is 12.

In the process of solving second-order differential equations, assembly vectors are employed:

$$Q_x = \begin{bmatrix} q_x \\ \dot{q}_x \end{bmatrix}, Q_y = \begin{bmatrix} q_y \\ \dot{q}_y \end{bmatrix}; \dot{Q}_x = \begin{bmatrix} \dot{q}_x \\ \ddot{q}_x \end{bmatrix}, \dot{Q}_y = \begin{bmatrix} \dot{q}_y \\ \ddot{q}_y \end{bmatrix}.$$

Consequently, using equation (6),  $\dot{X}$  and  $\dot{Y}$  are solved; and then from equation (7),  $\ddot{X}_r$  and  $\ddot{Y}_r$  are solved. The resulting vectors are as follows:

$$\dot{Q}_x = \begin{bmatrix} \dot{X} \\ \dot{X}_r \\ \ddot{X} \\ \ddot{X}_r \end{bmatrix}, \dot{Q}_y = \begin{bmatrix} \dot{Y} \\ \dot{Y}_r \\ \ddot{Y} \\ \ddot{Y}_r \end{bmatrix}$$

Only the assembled solution vector can be used for the integral solution of differential equations.

Formulas (6) ~ (7) demonstrate that obtaining the oil film force of the floating ring bearing in the inner and outer layers is a prerequisite for determining the dynamic characteristics of the rotor system of the floating ring bearing. Therefore, the Capone nonlinear oil film force model is required to calculate the oil film force of the floating ring bearing in the inner and outer layers.

These equations describe how the system will respond and move under the influence of external forces and internal stiffness. The model takes into account the elastic deformation of the rotor shaft, making it more complex and involving more parameters. It comprises a total of four centralized mass nodes and 12 degrees of freedom. Therefore, the Centralized Mass Model is more accurate and better suited to simulate and predict system dynamic behavior compared to the simple Jeffcott Model. Overall, the Centralized Mass Model provides a valuable tool for gaining insights into system behavior while avoiding some of the complexities associated with real-world structures. It's important to note, however, that this model is an approximation, and its accuracy might decrease for systems with more complex mass distributions or interactions.

### 2.2.2 Oil film force of floating ring bearing

The system equation of the TRS requires the calculation of lubrication force, which results from the lubrication pressure in the revolute ring bearing. A typical approach for calculating the lubrication pressure of revolute bearings is the Capone model.

Based on Capone nonlinear oil film force model, the difference in oil film force between the inner and outer layers of floating ring bearing lies in speed  $\omega$ . Obviously, for the outer oil film, the speed is  $\omega = \omega_r$ ; while for the inner oil film, because the journal and the floating ring rotate at the same time, the speed  $\omega = \omega_j + \omega_r$ .

Therefore, the oil film pressure on the outer layer of the floating ring bearing is given by:

$$p_o = \frac{3\mu}{h^3} \left( z^2 - \frac{L^2}{4} \right) [(\omega_r x - 2\dot{y}) \sin \theta - (\omega_r y + 2\dot{x}) \cos \theta] \quad (8)$$

The oil film pressure on the inner layer of the floating ring bearing is:

$$p_i = \frac{3\mu}{h^3} \left( z^2 - \frac{L^2}{4} \right) [((\omega_r + \omega_j)x - 2\dot{y}) \sin \theta - ((\omega_r + \omega_j)y + 2\dot{x}) \cos \theta] \quad (9)$$

In these equations,  $\mu$  represents the dynamic viscosity of the lubricating oil,  $h$  represents the thickness of the lubricating oil film,  $z$  is related to the position along the vertical axis.  $L$  represents the length of the bearing.  $\omega_r$  denotes the angular velocity of one of the surfaces in contact, influencing the pressure distribution in the oil film due to the relative rotation.  $x$  and  $y$  represent coordinates in a two-dimensional space, describing the relative motion of the surfaces along the x and y directions.  $\theta$  denotes the azimuth angle.

As a result, according to the pressure equations, by obtained by numerical integration, we got the oil film force obtained from the oil film pressure:

$$\begin{cases} f_x = \sum_{i=1}^m \sum_{j=1}^n p_{i,j} \cdot \Delta B \cdot \Delta \theta \cdot R \cdot \cos \theta \\ f_y = \sum_{i=1}^m \sum_{j=1}^n p_{i,j} \cdot \Delta B \cdot \Delta \theta \cdot R \cdot \sin \theta \end{cases} \quad (10)$$

$f_x$  and  $f_y$  represent the total forces acting along the x-direction and y-direction on the planar area,



respectively.  $m$  and  $n$  are the numbers of circumferential and axial elements, respectively.  $p_{i,j}$  represents the pressure at a specific grid point  $(i, j)$  on the planar area.  $\Delta B$  and  $\Delta \theta$  represents the unit lengths are circumferential and axial directions, respectively.  $R$  is the radial distance from the origin to a specific grid point  $(i, j)$  on the planar area.

$f_x$  is the sum of all the forces acting along the x-direction on the planar area. It is obtained by summing up the contributions of pressure  $p_{i,j}$  at each grid point  $(i, j)$  on the planar area. The contribution of each grid point is scaled by the changes in radial direction ( $\Delta B$ ), the angular direction ( $\Delta \theta$ ), the radial distance ( $R$ ), and the cosine of the angle  $\theta$ .

$f_y$  is the sum of all the forces acting along the y-direction on the planar area. It is obtained by adding up the pressure contributions at each grid point  $(i, j)$  on the planar region, denoted as  $p_{i,j}$ . The contribution of each grid point's is scaled by the sine of the angle, the radial distance ( $R$ ), the change in angular direction ( $\Delta B$ ), the change in radial direction ( $B$ ), and the change in radial direction ( $\Delta \theta$ ).

In summary, these expressions represent a discrete approximation for calculating the total forces acting on a planar area using pressure data at grid points in polar coordinates.

### 2.2.3 Solving Lubricating model

For solving Lubricating model mentions earlier, we choose to use tool 'ODE15s' to find the solve for the function. ODE15s is particularly suited to problems where the stiffness of the equations is important. Firstly, since Lubrication models sometimes involve differential equations with large changes in time scales, when the time scale varies greatly, the system becomes stiff, and ODE15s is suitable for such cases because it is effective in handling stiff systems. Secondly, this tool is known for its high accuracy. ODE15s utilizes variable step size and variable order techniques to ensure accurate solutions. This is especially important in lubrication modeling where accurate results are critical. Thirdly, ODE15s can dynamically adjust the step size based on the stiffness and behavior of the equations. This adaptive step size is useful in lubrication models where the stiffness may change when surfaces are close together or apart.

## 3. Model Analysis

Table 1: Variables of TRS

Bearing span $A$	32.3 mm	Bearing span $B$	35.3 mm
Bearing span $F$	30.1 mm	Shaft diameter $D_1$	14(-0.0067~0)mm
Floating ring bearing inner diameter $D_2$	14(+0.040~+0.045)mm	Floating ring bearing outer diameter $D_3$	20.7(-0.080~-0.070)mm
Bearing seat inner diameter $D_4$	20.7(0~+0.011)mm	Bearing width $E$	16.5 mm
Bearing width $M_c$	0.204 kg	Bath wheel mass $M_t$	0.796 kg
Impeller eccentricity (backdisk) $M_{ecb}$	0.4 g * mm	Impeller eccentricity (nose) $M_{ecn}$	0.4 g * mm
Turbine eccentricity (backdisk) $M_{etb}$	0.6 g * mm	Turbine eccentricity (nose) $M_{etn}$	0.6 g * mm



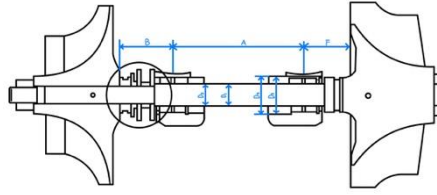


Figure 6: Defined Variables in TRS diagram

In this part, it is going to use data above (Table 1) and ‘ODE15’ method of MATLAB to draw four kinds of diagrams, which are Bifurcation Diagram, Poincare map, Trace plot and Waterfall 3D Cascade Diagram. Here’s the functions of each diagram:

A Bifurcation Diagram is a diagram that displays the possible long-term changes in system behavior when the value of the control parameter is varied [3]. In this analysis, the x-axis represents the rotational speed of the system, and the y-axis represents the distance of bearing ring from the center. From the diagram, it shows the states of the system — whether it is in a stable state or an unstable state in the cycle.

A Poincare map is the approach allows to identify patterns, periodicities, and irregularities within the system's behavior, aiding in the design, analysis, and optimization of various engineering systems, from mechanical components to control systems and beyond.

A Trace plot is the three-dimensional graph used to describe the trace of the bearing ring moving around the axis. From the graph, the amplitude of ring’s moving motion is clear, which helps provide a better description on the motion.

A Waterfall 3D Cascade Diagram has three axes – amplitude, rotational speed and frequency. It is uses to judge the number of times frequency doubling occurs and to identity problems within the systems due to different times of frequency doubling. This is convenient for identifying and solving the problems of the system.

In modeling the turbocharger rotor system (Fig 6 shows defined variables in the system), we choose the outer diameter ( $D_3$ ) of the floating ring bearing as the variable. Here are the results of five different  $D_3$  values.

**Group 1:  $D_3 = 15.8$**

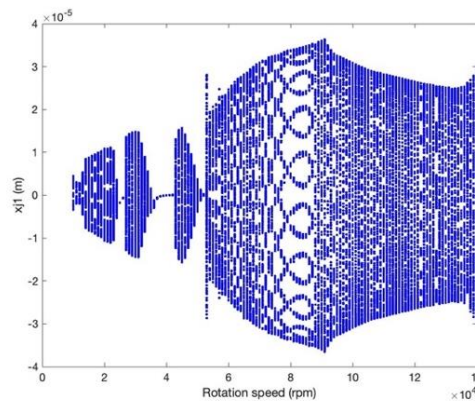


Figure 7: Bifurcation diagram from 10000rpm to 140000rpm of rotational speed

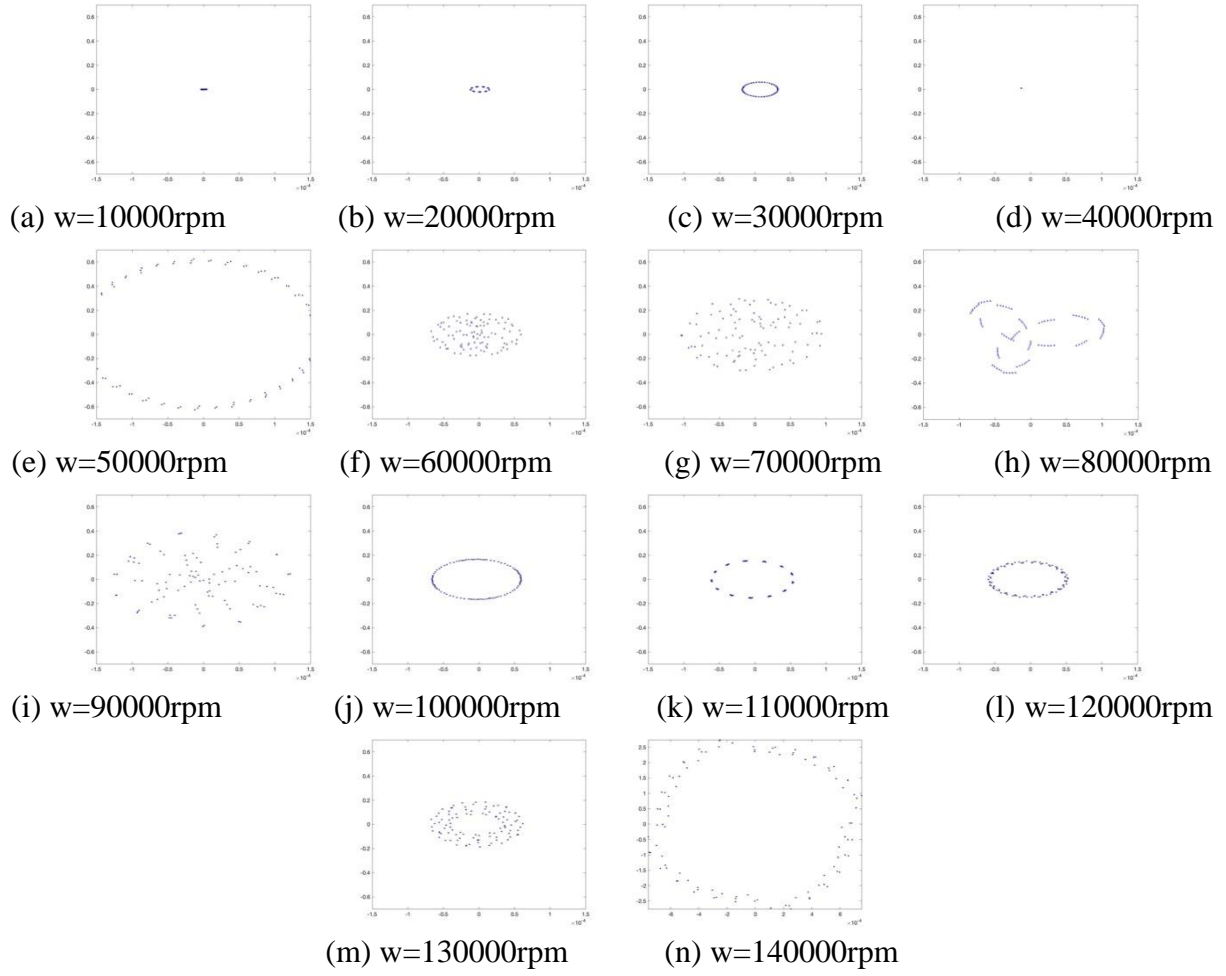
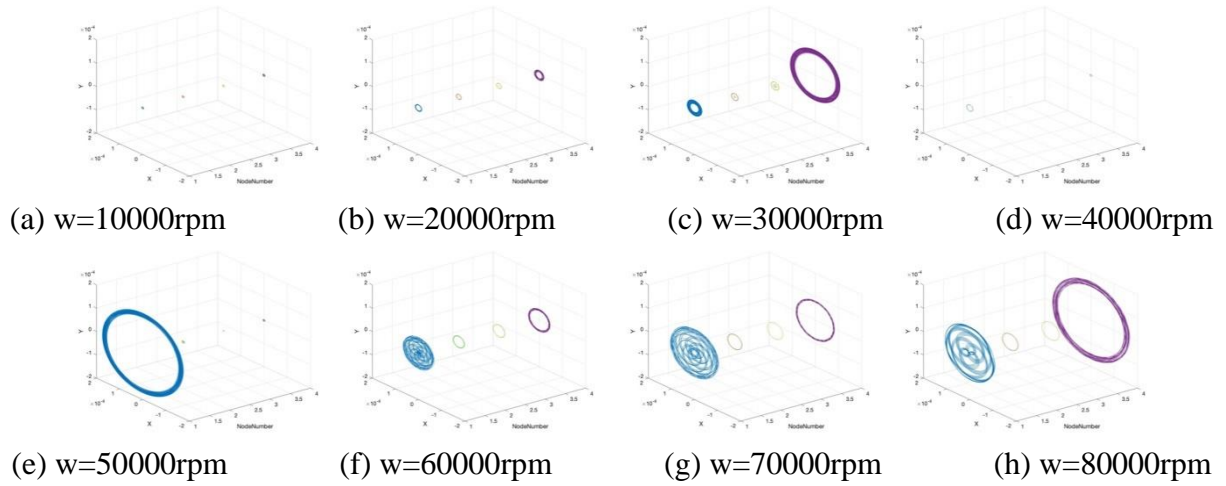


Figure 8: Poincaré mapping of the system at different speeds

According to the Bifurcation diagram and Poincaré mapping, as shown in Fig 7 and Fig 8, the motions is almost periodic from 10000rpm to 30000rpm; becoming periodic at 40000rpm, and turns chaotic during 50000rpm to 140000rpm.



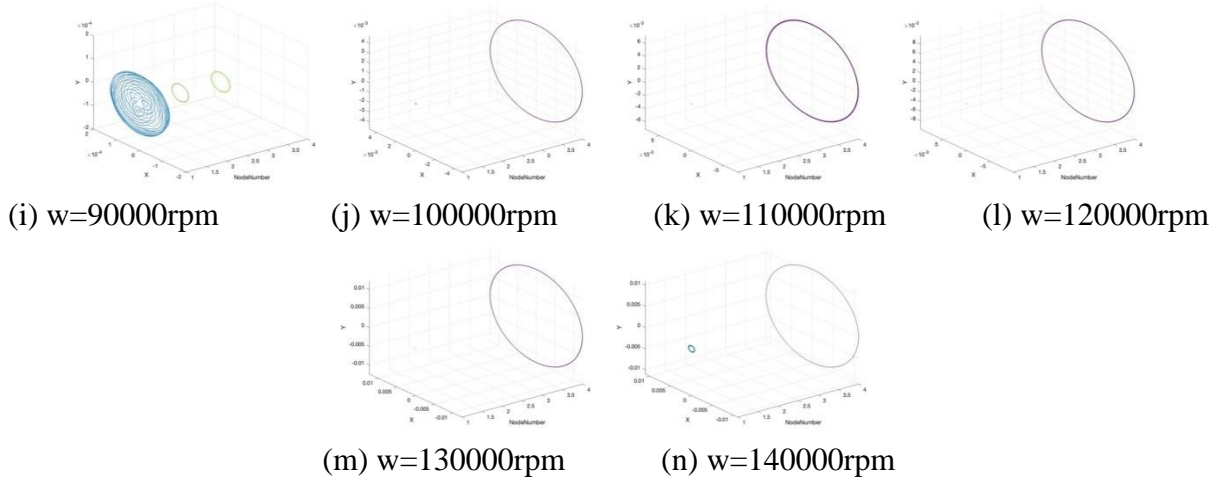


Figure 9: 3D trajectory map of the system at different rotational speeds

Based on the analysis results of the bifurcation diagram and Poincare diagram, it can be observed from the operating range shown in Fig 9 that within the range of 50000rpm~90000rpm, the system exhibits chaotic behavior, and the vibration amplitude of the left end plate is significantly larger compared to adjacent nodes. From 100000rpm~140000rpm, the vibration amplitude of the right end plate is relatively large compared to adjacent nodes. If it operates under these conditions for an extended period, the shaft may experience irreparable deformation, ultimately leading to the failure of the entire rotor system.

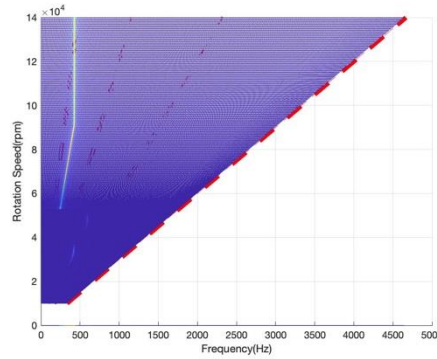


Figure 10: Waterfall 3D Cascade Diagram

The Waterfall 3D Cascade graph, as shown in Fig 10, demonstrates that fundamental frequency doubling occurs when the system rotational speed reaches approximately 23000 rpm; at around 30000 rpm, half-frequency doubling occurs, the inner oil film is destroyed, and conical vortex motion takes place. The half frequency doubling, which is also a sign of the system's instability, persists until 38000 rpm before briefly disappearing and reappearing at 43000 rpm. The half-frequency doubling remains present up to 50000rpm. 0.15 frequency doubling first emerges about 52000 rpm and lasts until 140000 rpm. Thus, this system of radius 15.8 is not very effective.

**Group 2:  $D_3 = 17.3$**

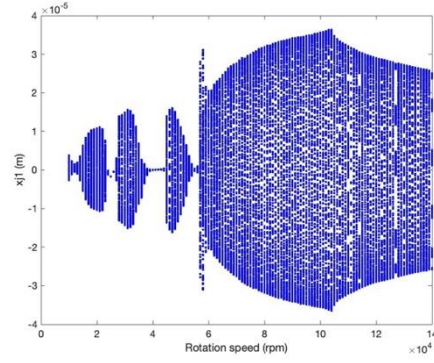


Figure 11: Bifurcation diagram from 10000rpm to 140000rpm of rotational speed

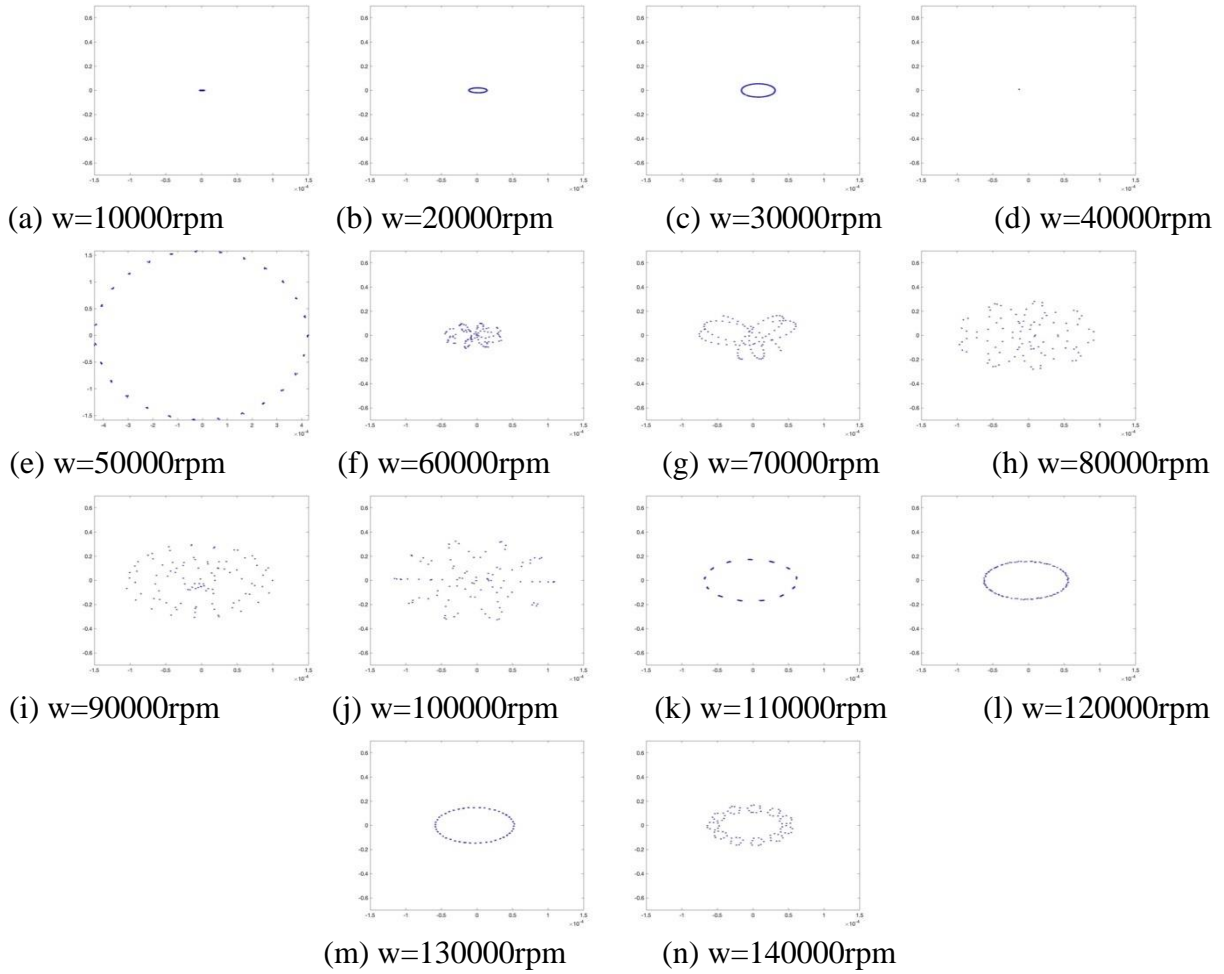


Figure 12: Poincaré mapping of the system at different speeds

According to the Bifurcation diagram and Poincaré mapping, as shown in Fig 11 and Fig 12, the motion is almost periodic from 10000rpm to 50000rpm; becomes chaotic during 60000rpm to 100000rpm, returns to almost periodic from 110000rpm to 130000rpm, and finally, at the fastest rotational speed of 140000rpm, the system becomes chaotic.

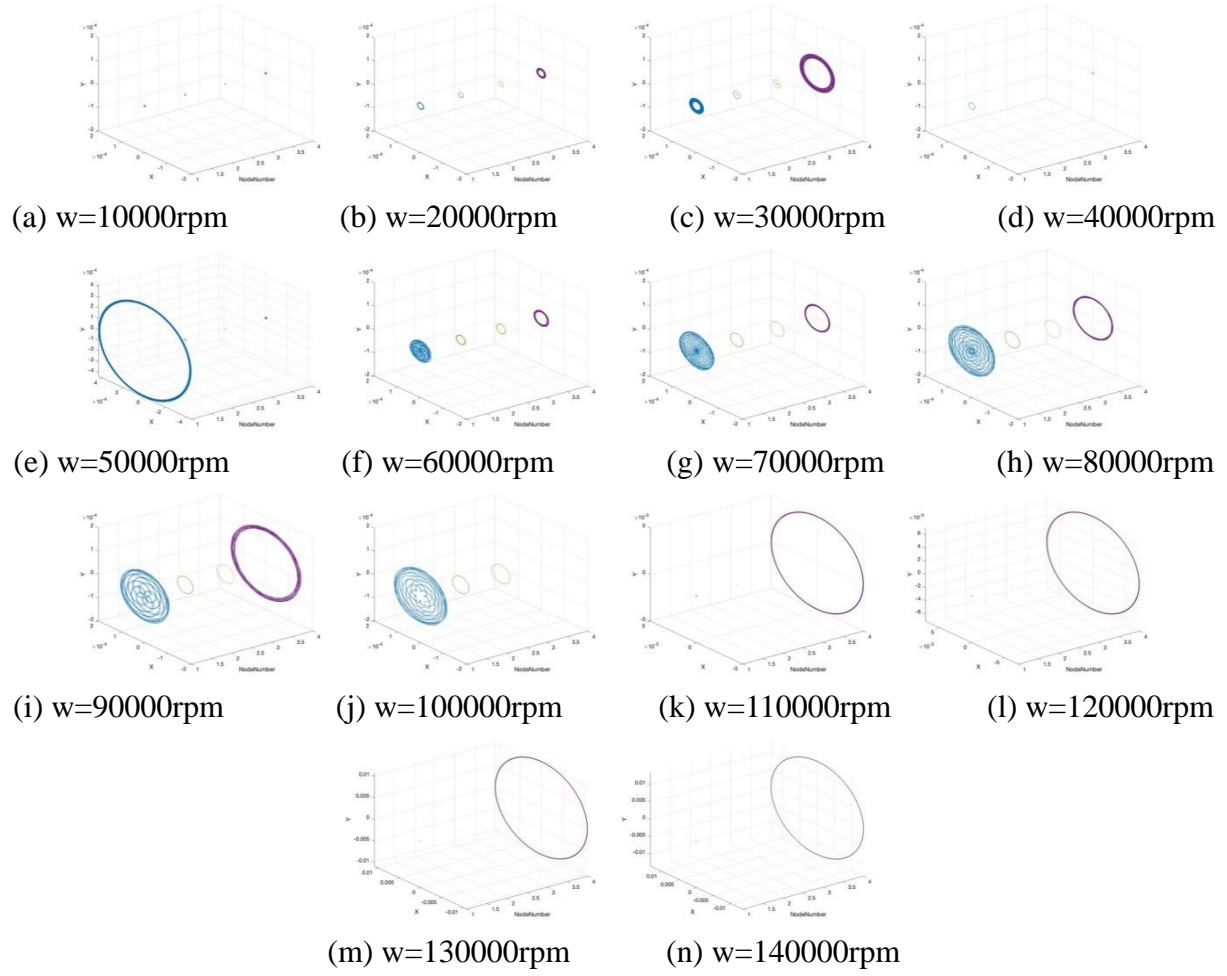


Figure 13: 3D trajectory map of the system at different rotational speeds

Based on the analysis results of the bifurcation diagram and Poincare diagram, it can be observed from the operating range shown in Fig 13 that within the range of 10000rpm~30000rpm and 110000rpm to 130000rpm, the system exhibits almost periodic motion. However, during the interval of 110000rpm to 130000rpm, the vibration amplitude of the right end plate is relatively large compared to adjacent nodes. If it operates under these conditions for an extended period, the shaft will experience irreparable deformation, ultimately leading to the failure of the entire rotor system.

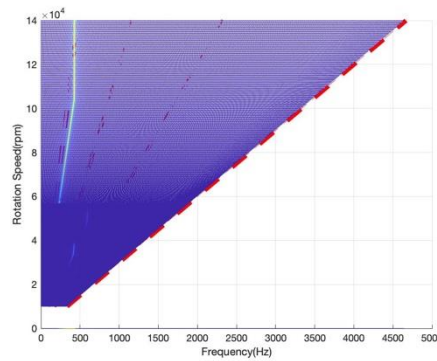


Figure 14: Waterfall 3D Cascade Diagram

According to Waterfall 3D Cascade diagram (Fig 14), it shows that when the system rotational speed reaches about 23000rpm, basic frequency doubling appears; and the speed reaches about

30000rpm, the half frequency doubling occurs, resulting in the damage of the inner oil film and the onset of conical vortex motion. At 40000rpm, the half frequency doubling disappears for a short time and reoccurs around 46000rpm, which is also the sign of lacking of stability of the system. It continues until 55000rpm when the half frequency doubling disappears. Around 58000rpm, 0.15 frequency doubling appears and ends at 140000rpm at last. Thus, this system with a radius 17.3 is not very effective.

**Group 3:  $D_3 = 20.7$**

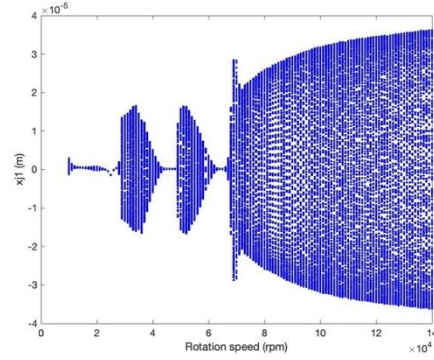


Figure 15: Bifurcation diagram from 10000rpm to 140000rpm of rotational speed

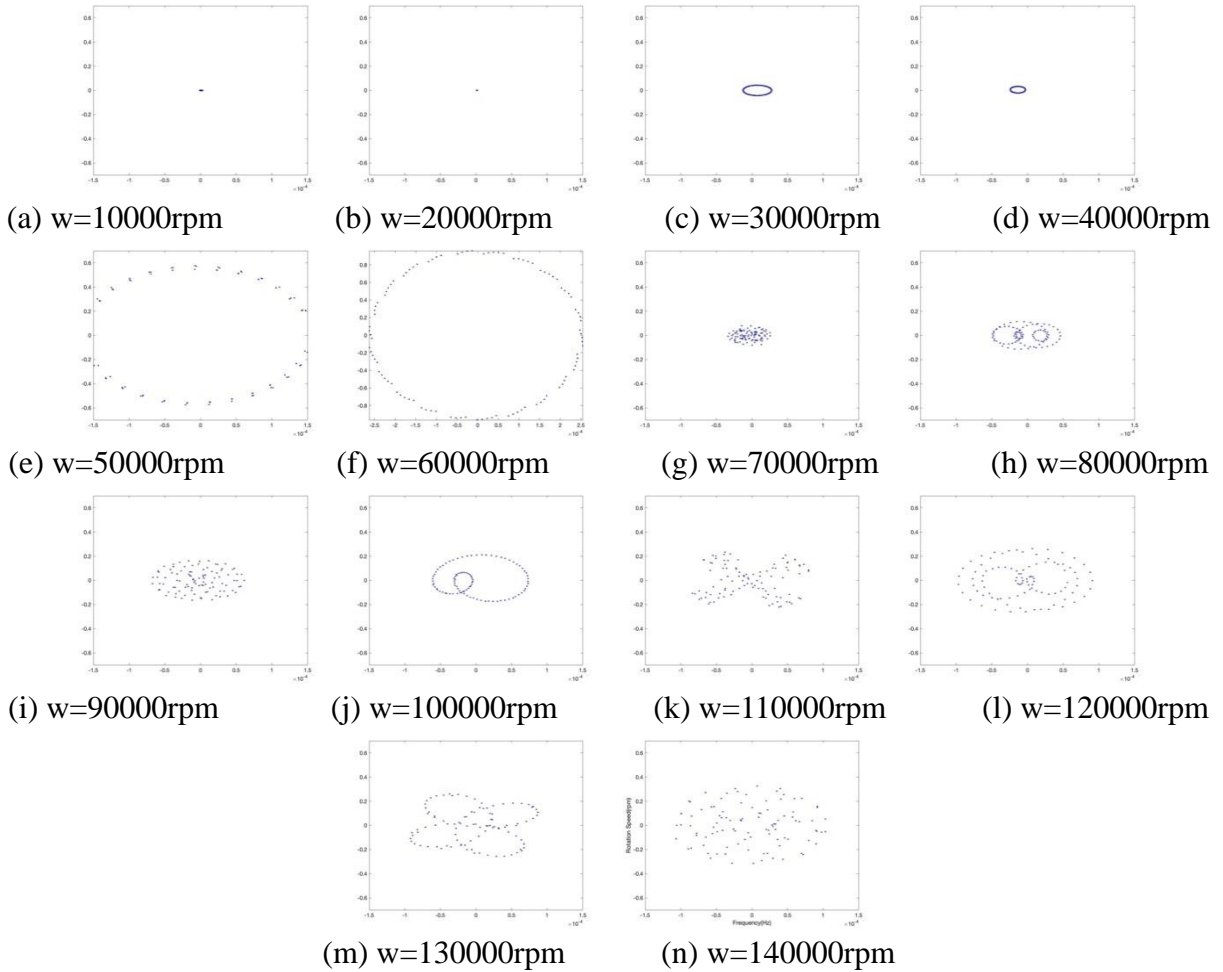


Figure 16: 3D trajectory map of the system at different rotational speeds

According to the Bifurcation diagram and Poincare mapping, as shown in Fig 15 and Fig 16, during



10000rpm to 20000rpm is periodic motion; during 30000rpm to 60000rpm, the motion of the system is almost periodic; then, during 70000rpm to 140000rpm, the system becomes chaotic.

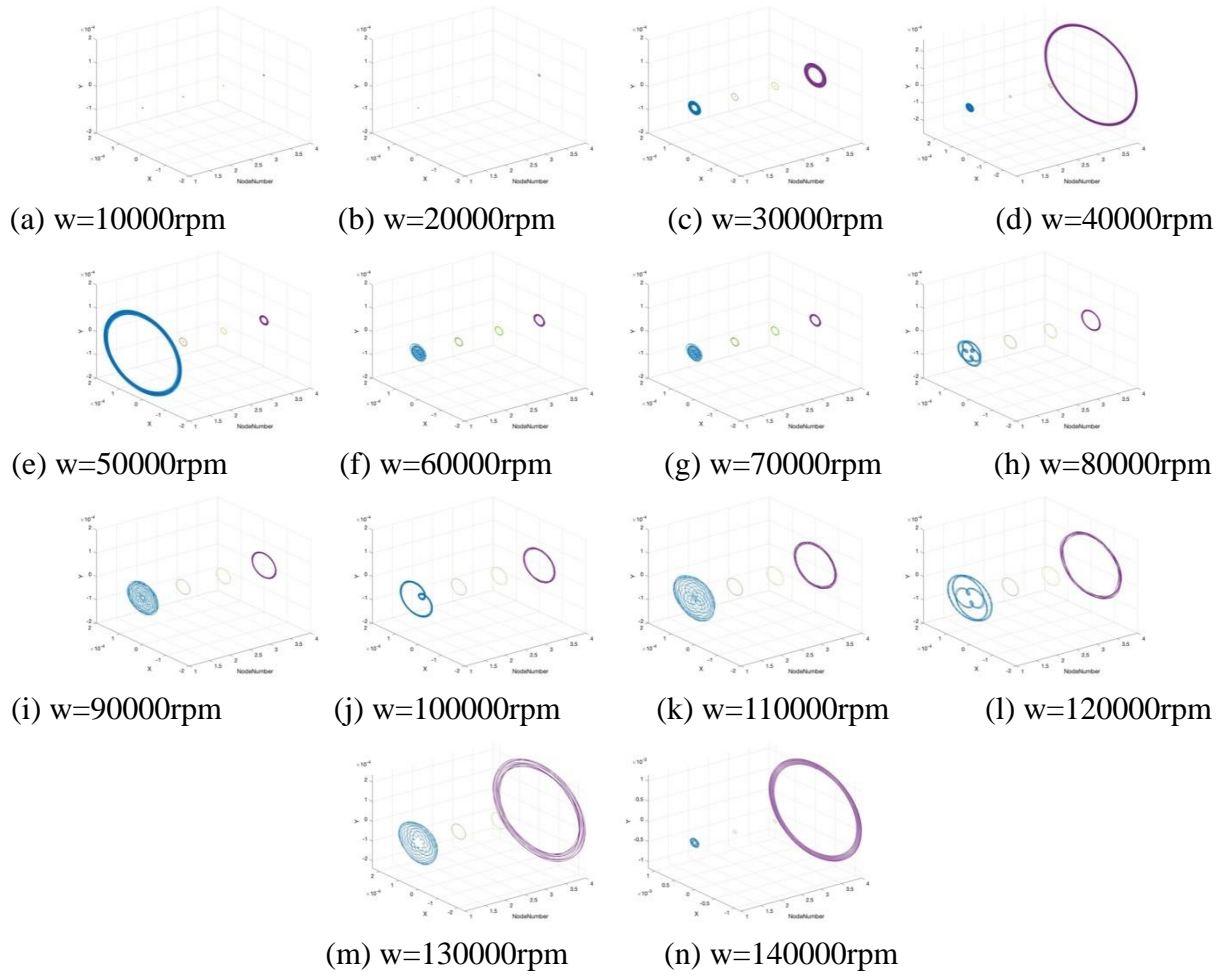


Figure 17: 3D trajectory map of the system at different rotational speeds

Based on the analysis of the bifurcation diagram and Poincare diagram, it is evident from the operating range in Fig 17 that the system exhibits almost periodic motion between 30000 and 60000 rpm, with acceptable vibration amplitudes in the left and right end plates. Therefore, this system can operate effectively. Furthermore, during the interval of 10000rpm to 20000rpm, the motion is perfectly stable.

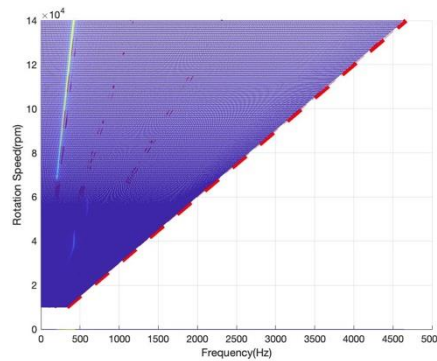


Figure 18: Waterfall 3D Cascade Diagram

According to Waterfall 3D Cascade diagram (Fig 18), it shows that when the system rotational



speed reaches about 23000rpm, basic frequency doubling appears, and when the speed reaches about 30000rpm, half frequency doubling occurs. It disappears briefly until 43000rpm and then reoccurs around 51000rpm. It continues until 60000rpm when the half frequency doubling disappears. Around 63000rpm, 0.15 frequency doubling appears and persists until 140000rpm. So for this motion, the system is under good operation.

**Group 4:  $D_3 = 22.5$**

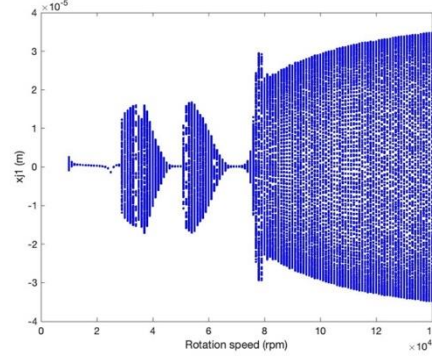


Figure 19: Bifurcation diagram from 10000rpm to 140000rpm of rotational speed

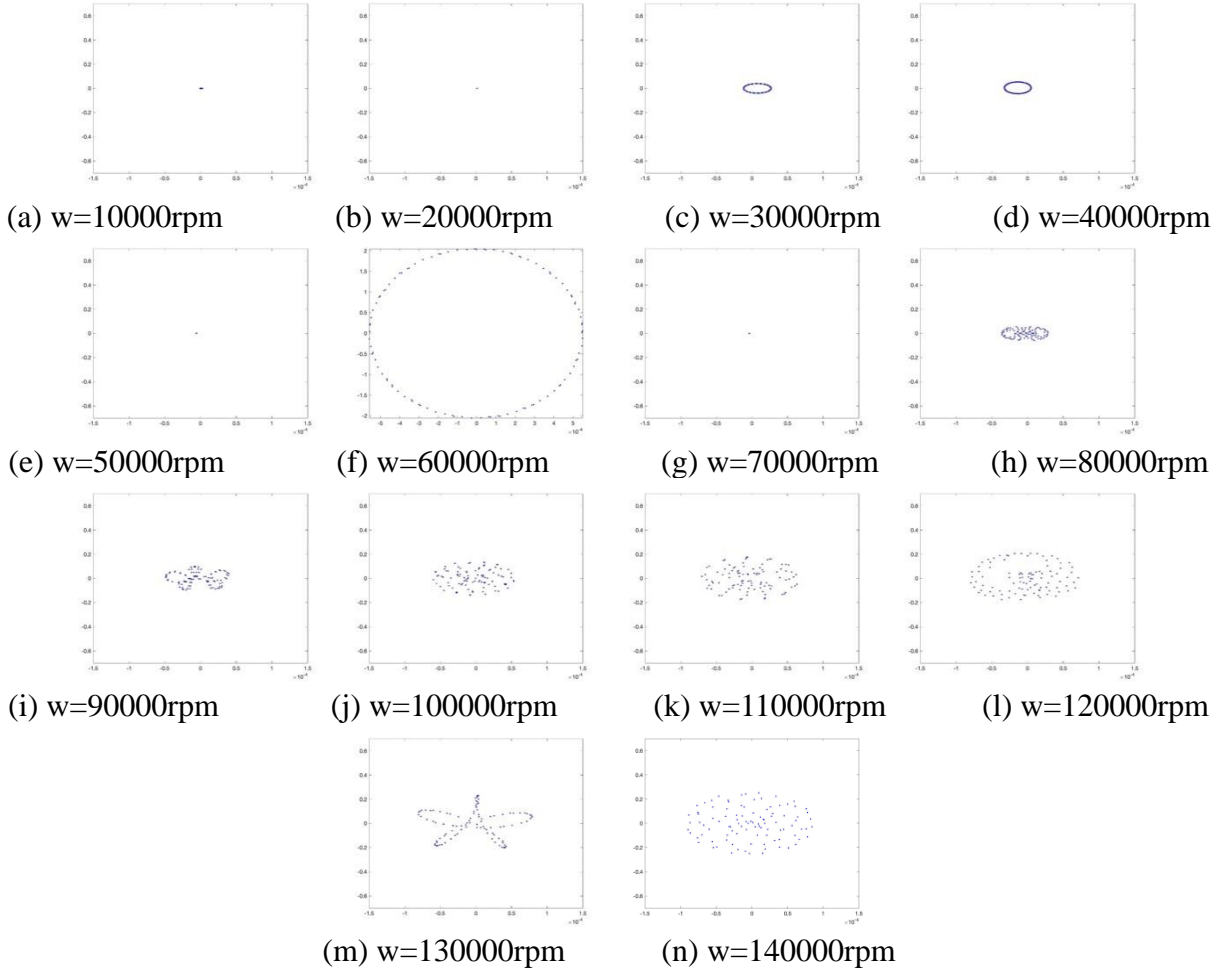


Figure 20: Poincare mapping of the system at different speeds

According to the Bifurcation diagram and Poincaré mapping, as shown in Fig 19 and Fig 20, during 10000rpm to 20000rpm is periodic motion; during 30000rpm to 40000rpm, the motion of the system

is almost periodic; then, during 50000rpm and 70000rpm, the system becomes periodic again; however, from 80000rpm to 140000rpm, the system becomes chaotic.

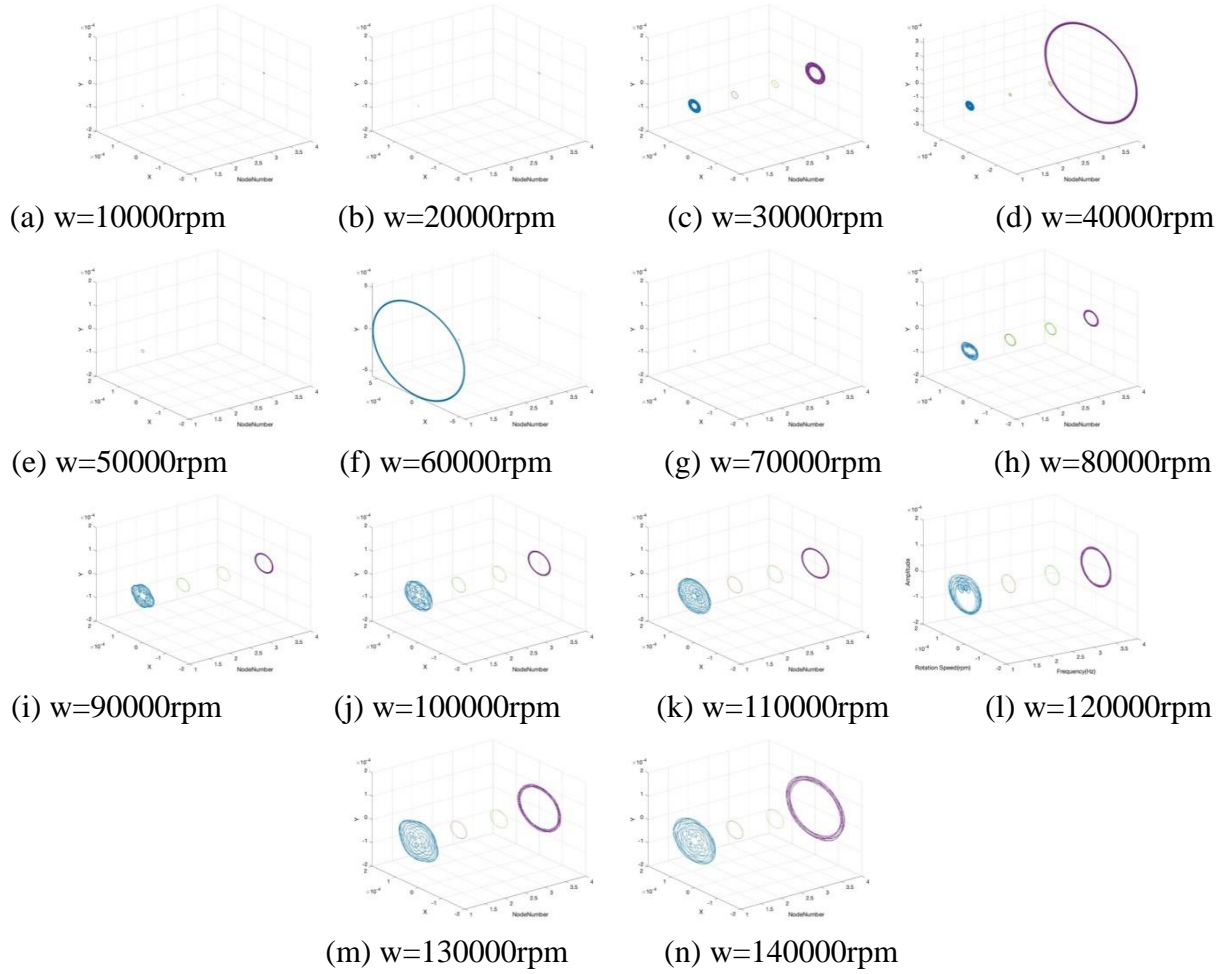


Figure 21: 3D trajectory map of the system at different rotational speeds

Based on the analysis results of the bifurcation diagram and Poincare diagram, it can be seen from the operating range shown in Fig 21 that within the range of 30000rpm to 40000rpm and 60000 rpm, the system is in almost periodic motion, but the vibration amplitude of the left end plate is relatively large compared to adjacent nodes, especially at 40000rpm and 60000rpm. But for rest of the rotational speed, the system is working quite good for their trajectory.

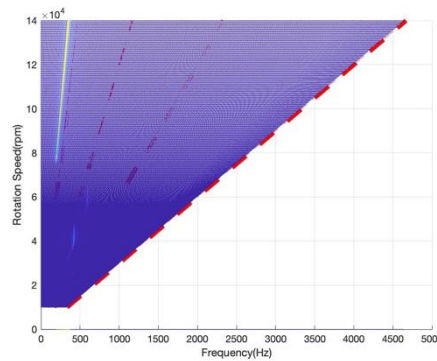


Figure 22: Waterfall 3D Cascade Diagram

According to Waterfall 3D Cascade diagram (Fig 22), it shows that when the system rotational

speed reaches approximately 23000rpm, basic frequency doubling occurs. As the speed approaches 30000rpm, the half frequency doubling emerges. It temporarily disappears around 44000rpm but reoccurs near 46000rpm. The half frequency doubling disappears again until approximately 63000rpm. At around 80000rpm, 0.15 frequency doubling becomes noticeable and continues until 140000rpm. The occurrence of half frequency doubling is brief, indicating that the system is in good condition and operate normally.

**Group 5:  $D_3 = 25.2$**

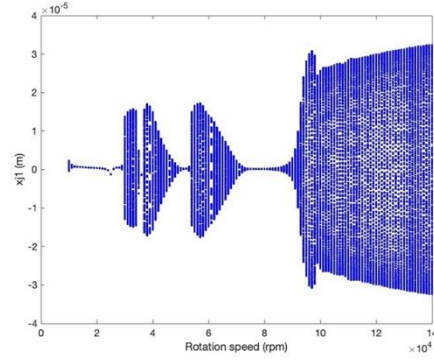


Figure 23: Bifurcation diagram from 10000rpm to 140000rpm of rotational speed

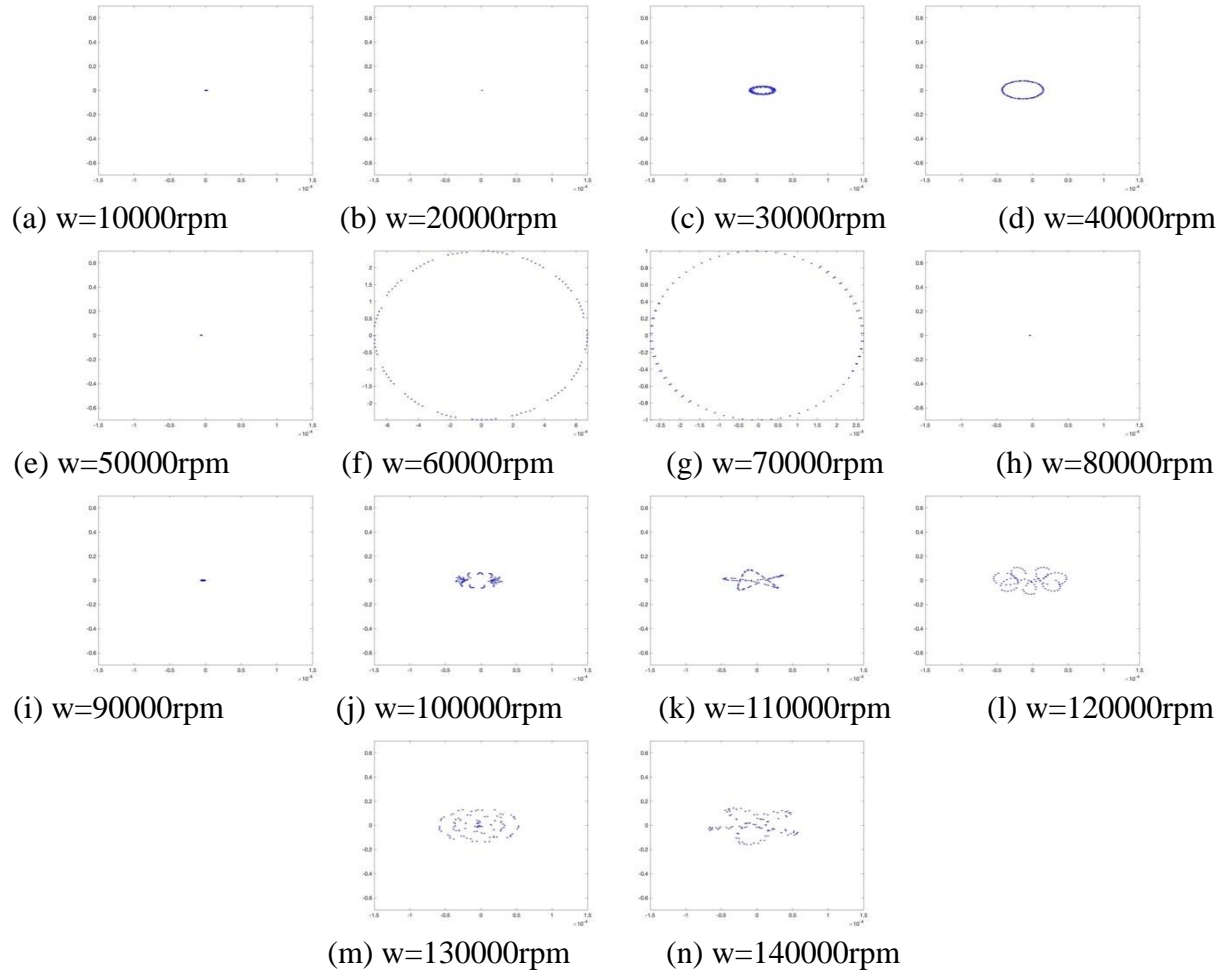


Figure 24: Poincaré mapping of the system at different speeds

According to the Bifurcation diagram and Poincaré mapping, as shown in Fig 23 and Fig 24, during

10000rpm to 20000rpm is periodic motion; during 30000rpm to 50000rpm and 80000rpm to 90000rpm, the motion of the system is almost periodic; then, during 60000rpm to 70000rpm, the system becomes periodic again. However, from 100000rpm to 140000rpm, the system becomes chaotic.

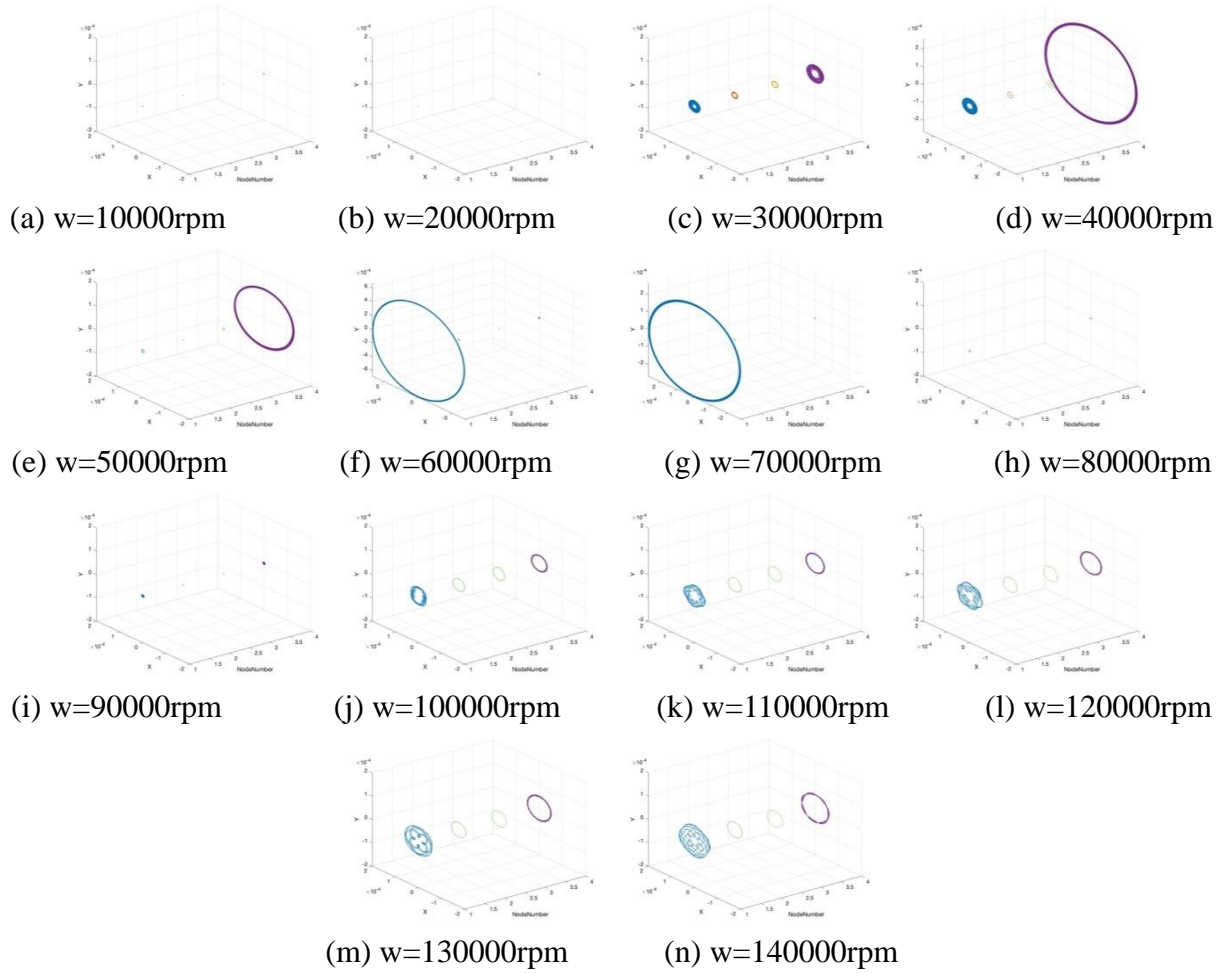


Figure 25: 3D trajectory map of the system at different rotational speeds

Based on the analysis of the bifurcation diagram and Poincare diagram, it is evident from the operating range in Fig 25 that the system is in almost periodic motion between 30000 and 50000 rpm, and 80000rpm to 90000rpm. However, the vibration amplitude of the right end plate is relatively high in comparison to nearby nodes for 30000 and 50000 rpm. But for interval of 80000rpm to 90000rpm, the system is really stable under operation.

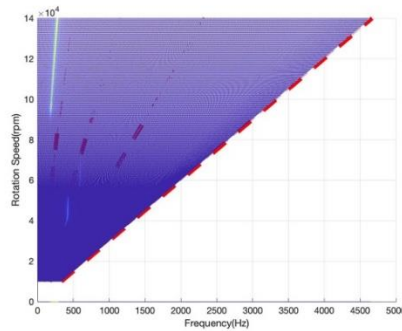


Figure 26: Waterfall 3D Cascade Diagram

The Waterfall 3D Cascade diagram (Fig 26) demonstrates that fundamental frequency doubling develops when the system rotational speed reaches about 23000 rpm; at about 38000 rpm, half frequency doubling arrives. The half frequency doubling, which is also a sign of the system's instability, lasts until 51000 rpm before briefly disappearing and reappearing about 58000 rpm. The half frequency doubling remains present up until 69000rpm. A 0.15 frequency doubling starts to appear about 90000 rpm and lasts until 140000 rpm. Therefore, the interval of 80000rpm to 90000rpm is the perfect interval.

#### 4. Conclusion

In summary, from the comparison of different sets of data and graphs, the system performs best at speeds ranging from 70000rpm to 80000rpm. For the outer diameter of the variable rotor, according to the results, the larger the outer radius, the better the system performance, and it performs excellently in the range of 22.5 to 25.2, while outer radius values smaller than this are more like to not be useful due to oil film whirl or oil film oscillation or some other reasons.

#### References

- [1] Liu, Z., Wang, R., Cao, F., & Shi, P. (2020). *Dynamic Behaviour Analysis of Turbocharger Rotor-Shaft system in thermal environment based on finite element method*. *Shock and Vibration*, 2020, 1–18. <https://doi.org/10.1155/2020/8888504>
- [2] Saeed, N.A., Kamel, M. Active magnetic bearing-based tuned controller to suppress lateral vibrations of a nonlinear Jeffcott rotor system. *Nonlinear Dyn* 90, 457–478 (2017). <https://doi.org/10.1007/s11071-017-3675-y>
- [3] Pham, V.-T., Volos, C., & Vaidyanathan, S. (2015). Chaotic Attractor in a Novel Time-Delayed System with a Saturation Function. In *Handbook of Research on Advanced Intelligent Control Engineering and Automation* (pp. 29). doi:10.4018/978-1-4666-7248-2.ch008
- [4] Tammineni, N.M., Mutra, R.R. A review on recent advancements in an automotive turbocharger rotor system supported on the ball bearings, oil film and oil-free bearings. *J Braz. Soc. Mech. Sci. Eng.* 45, 481 (2023). <https://doi.org/10.1007/s40430-023-04383-8>
- [5] Genta, G. (2005). Jeffcott rotor. In: *Dynamics of Rotating Systems. Mechanical Engineering Series*. Springer, New York, NY. [https://doi.org/10.1007/0-387-28687-X\\_2](https://doi.org/10.1007/0-387-28687-X_2)
- [6] Ding, Q., Leung, A.Y.T. (2005). Numerical and Experimental Investigations on Flexible Multi-bearing Rotor Dynamics. *Journal of Vibration and Acoustics*, 127(4). doi:10.1115/1.1898336
- [7] Ding, Q., Cooper, J., & Leung, A. Y. T. (2002). Hopf bifurcation analysis of a rotor/seal system. *\*Journal of Sound and Vibration*, 252\*, 817-833. doi:10.1006/jsvi.2001.3711.
- [8] Wang, Y., & Wang, X. (2010). Nonlinear Vibration Analysis for a Jeffcott Rotor with Seal and Air-Film Bearing Excitations. *Mathematical Problems in Engineering*, 2010. doi:10.1155/2010/657361.
- [9] Friswell, M., Penny, J., Garvey, S., & Lees, A. (2010). More complex rotordynamic models. In *Dynamics of Rotating Machines*.
- [10] Capone, G. (1991). Analytical description of the fluid dynamic force field in lubricated cylindrical bearings. *\*The Electric Power\**, 3, 105-110.